10342–10352 *Nucleic Acids Research, 2020, Vol. 48, No. 18* *Published online 7 September 2020*
doi: 10.1093/nar/gkaa733

Hedgehog signaling enables repair of ribosomal DNA double-strand breaks

Tshering D. Lama-Sherpa [1,†], Victor T.G. Lin [2,3,†], Brandon J. Metge[1], Shannon E. Weeks[1], Dongquan Chen[3,4], Rajeev S. Samant [1,3,5] and Lalita A. Shevde [1,3,*]

[1]Department of Pathology, The University of Alabama at Birmingham, Birmingham, AL, USA, [2]Division of Hematology and Oncology, Department of Medicine, The University of Alabama at Birmingham, Birmingham, AL, USA, [3]O'Neal Comprehensive Cancer Center, The University of Alabama at Birmingham, Birmingham, AL, USA, [4]Division of Preventative Medicine, Department of Medicine, The University of Alabama at Birmingham, Birmingham, AL, USA and [5]Birmingham VA Medical Center, Birmingham, AL, USA

Received March 03, 2020; Revised August 20, 2020; Editorial Decision August 21, 2020; Accepted September 04, 2020

ABSTRACT

Ribosomal DNA (rDNA) consists of highly repeated sequences that are prone to incurring damage. Delays or failure of rDNA double-strand break (DSB) repair are deleterious, and can lead to rDNA transcriptional arrest, chromosomal translocations, genomic losses, and cell death. Here, we show that the zinc-finger transcription factor GLI1, a terminal effector of the Hedgehog (Hh) pathway, is required for the repair of rDNA DSBs. We found that GLI1 is activated in triple-negative breast cancer cells in response to ionizing radiation (IR) and localizes to rDNA sequences in response to both global DSBs generated by IR and site-specific DSBs in rDNA. Inhibiting GLI1 interferes with rDNA DSB repair and impacts RNA polymerase I activity and cell viability. Our findings tie Hh signaling to rDNA repair and this heretofore unknown function may be critically important in proliferating cancer cells.

INTRODUCTION

Ribosomal DNA (rDNA) comprises repeated sequences encoding the 45S and 5S ribosomal RNAs (rRNAs) that form the basis of ribosome structure and function (1). These regions of chromatin are open and highly transcribed in actively proliferating cells in order to match their extensive metabolic demands, making them prone to incurring damage (2–4). Genome-wide mapping of DSBs shows a predilection for rDNA that leads to genomic rearrangements (2). Thus, chromosomal translocations in rDNA are among the most common genomic alterations in adult solid tumors (4). Delayed, erroneous, or incomplete repair of double-strand breaks (DSBs) in these loci can lead to deleterious chromosomal translocations, genomic instability, aneuploidy, and ultimately mitotic catastrophe and cell death (5–7).

Cells have two major repair mechanisms in place to resolve DSBs: homologous recombination (HR) and non-homologous end joining (NHEJ). HR is cell cycle-dependent and results in high-fidelity repair of DSBs, whereas NHEJ is cell cycle-independent and comprises blunt end-joining that is more immediate but more error-prone (8). NHEJ is the preferred repair pathway for rDNA DSBs (9), though they may also be resolved by HR machinery independent of the cell cycle as a contingency (10). Errors in repair can lead to loss of repeats and chromosomal translocations involving 45S rDNA loci, which are found on five different chromosomes (4). Delays in the resolution of rDNA DSBs result in the arrest of rDNA transcription by RNA polymerase I (Pol I) via an ATM-dependent mechanism (9). Unrepaired rDNA damage, especially of 45S rDNA, is deleterious (5). Thus, rDNA repair is an attractive target for novel cancer therapeutics.

We sought to investigate the role of Hedgehog (Hh) signaling in DNA repair. Previous work in our laboratory connected GLI1, a zinc-finger transcription factor that is a terminal effector of the Hh pathway, to the DNA single-strand break (SSB) repair via the nucleotide and base excision repair pathways (NER and BER). We showed that GLI1 upregulates expression of NER and BER genes in response to SSBs to facilitate their repair (11). Hh inhibition is also known to sensitize cancer cells to agents that induce DSBs, but the mechanisms by which Hh influences DSB repair are poorly understood (12,13). We hypothesized that induction of DSBs by ionizing radiation (IR) would result in cistromic changes in GLI1 in order to orchestrate the activation of DNA repair programs. Unexpectedly, we found that GLI1 occupancy of rDNA loci is markedly enriched in response to IR and that GLI1 is required for timely repair of rDNA DSBs.

*To whom correspondence should be addressed. Tel: +1 205 975 6261; Fax: +1 205 975 6615; Email: lalitasamant@uabmc.edu
†The authors wish it to be known that, in their opinion, the first two authors should be regarded as Joint First Authors.

MATERIALS AND METHODS

Cell culture

SUM1315 cells were cultured in DMEM/F12 (Gibco) containing 5% heat-inactivated FBS (Gibco), 10 μg/ml insulin (Sigma), and 25 ng/ml EGF (Sigma). MDA-MB-468 cells were cultured in DMEM/F12 containing 10% FBS. SUM159 cells were cultured in DMEM/F12 containing 5% FBS, 10 μg/ml insulin, and 1 μg/ml hydrocortisone (Sigma). Culture media were all free of antibiotics and antimycotics unless otherwise stated. Cells were maintained at 37°C in a humidified environment containing 5% CO_2.

Hh/GLI1 inhibition

Cells were treated with 10 μM vismodegib (SelleckChem) or 10 μM GANT61 (Tocris) solubilized in DMSO (Fisher) as stated in each figure. Unless otherwise noted, cells were treated with an inhibitor or vehicle control for 24 h prior to irradiation. Where noted, SUM1315 cells were stably transfected with either a non-targeted plasmid or shRNA directed against GLI1 as previously described (14) and maintained in selection with 300 μg/ml G418 (Gibco).

Ionizing radiation

Cells were irradiated with the indicated doses using the X-RAD 320 (Precision) X-ray irradiator with exposures quantified using the UNIDOS E dosimeter (PTW).

Chromatin immunoprecipitation and next-generation sequencing

SUM1315 cells were plated on 100 mm dishes (Corning). At approximately 90% confluence, they were either mock irradiated or irradiated with 4 Gy and crosslinked with 1% formaldehyde (Fisher) at room temperature at the indicated times after irradiation. Where indicated, cells were pre-treated with DMSO or 10 μM GANT61 beginning 24 h prior to irradiation. After crosslinking, cells were harvested for chromatin immunoprecipitation (ChIP) using the SimpleChIP Plus Kit with Magnetic Beads (Cell Signaling) according to manufaturer's protocol. Sonication was done with six 10-s pulses at 50% power using a FB-120 sonic dismembrator (Fisher), with 60-s rests on ice in between each pulse. After confirmation of shearing quality using agarose gel electrophoresis, 10 μg of crosslinked, sheared chromatin was used for each immunoprecipitation reaction, with 2% input controls saved for comparison. GLI1 ChIP was performed using 3 μg of C-1 antibody (Santa Cruz). For standard ChIP analysis, equal volumes of eluted DNA were used for quantitative PCR and normalized to C_T values of the corresponding 2% input control with the following formula: percent input = 2% × 2(C_T 2% input sample - C_T IP sample). Nonspecific signals calculated from beads only controls were subtracted from each corresponding IP. Primers used are tabulated in Supplementary Table S1. For ChIP-Seq, 2% input controls and eluted DNA from ChIP reactions done in duplicate were submitted to an external vendor (GENEWIZ) for next-generation sequencing. ChIP-Seq data was aligned to the hg19 genome using BWA Aligner (15). Peak calling was done using MACS2 (16) (https://github.com/taoliu/MACS/tree/master/MACS2) and filtered for peaks of interest between −5000 and +2000 of transcriptional start sites. ChIP-Seq peaks were visualized using the Integrative Genomics Viewer (17).

Immunoblotting

Cells were lysed in RIPA buffer (Millipore) containing HALT protease and phosphatase inhibitor cocktail (ThermoScientific) and sonicated to complete lysis. Lysates were clarified by centrifugation before protein concentrations were assayed using the Precision Red assay (Cytoskeleton). Equal masses were electrophoresed by SDS-PAGE and wet transferred to PVDF membranes (BioRad). When probing for proteins with molecular weights over 200 kDa, precast gradient gels were used (Invitrogen and BioRad) and wet transfers were done at 30 V for 16 h. Primary antibodies against γ-H2AX (Cell Signaling, 9718S), GLI1 (Cell Signaling, 2643S), fibrillarin (Cell Signaling, 2639S), I-SceI (Abcam, ab216263), 53BP1 (Cell Signaling, 4937S), phospho-53BP1 S1778 (Cell Signaling, 2675S), ATM (Cell Signaling, 2873S), phospho-ATM S1981 (Cell Signaling, 5883S), NBS1 (Cell Signaling, 3002S), phospho-NBS1 S343 (Cell Signaling, 3001S), and β-actin (Sigma) were used, as well as secondary HRP-conjugated antibodies against mouse and rabbit IgG (GE) when appropriate. Chemiluminescence images were captured using the Imager 600 (Amersham). Densitometry was calculated using ImageJ software (NIH).

Immunocytochemistry

Cells were plated on poly-L-lysine coated coverslips (Corning) in 35 mm dishes (Corning) at a seeding density of 300 000 cells per dish and were fixed with 4% paraformaldehyde (Sigma) for 30 min followed with two washes with ice-cold PBS (Corning). The fixed cells were permeabilized in 0.1% Triton X-100 (Fisher) in PBS (PBST) for 15 minutes followed by blocking in 5% BSA (Fisher) in PBST for 1 hour. Cells were incubated overnight at 4°C with 1:200 GLI1 (Cell Signaling, 2553S), 1:400 γ-H2AX (Cell Signaling, 9718S), 1:400 fibrillarin (Cell Signaling, 2639S), and 1:200 phospho-53BP1 S1778 (Cell Signaling, 2675S) primary antibodies in 5% BSA. Following three 10-min washes with PBS, cells were incubated in the dark with 1:100 secondary anti-mouse and anti-rabbit IgG antibodies conjugated to Alexa Fluor 488 and 594 (Invitrogen) in 5% BSA, followed by three 10-min washes in PBS before mounting with DAPI using VECTASHIELD (Vector Laboratories). Slides were visualized using an Eclipse TE2000-U microscope (Nikon) and representative images for γ-H2AX or phospho-53BP1 foci were captured at 100X magnification. Cells from 10 random fields were counted for analysis of γ-H2AX or phospho-53BP1 foci at 30X magnification. Cells were considered positive for γ-H2AX or phospho-53BP1 foci if 10 or more foci were identified. Intensity of GLI1-Fibrillarin co-localization was determined using the manufacturer's protocol for calculating binary intersection mean intensity in NIS-Elements (Nikon) software from five random 100X fields of similar cell density (∼10 cells per field).

Confocal microscopy

SUM1315 cells incubated for 1 h at room temperature with 1:200 GLI1 (Cell Signaling, 2553S) and 1:200 phospho-53BP1 S1778 (Cell Signaling, 2675S) primary antibodies in 5% BSA. After washing, cells were incubated in 1:100 secondary anti-mouse and anti-rabbit IgG antibodies conjugated to Alexa Fluor 488 and 594 (Invitrogen) in 5% BSA, followed by three washes in PBS before incubation for 1 h with 1:50 UBF Antibody (F-9) conjugated to Alexa Fluor 647 (Santa Cruz, sc-13125 AF647). The cells were stained with DAPI (Fisher) and mounted with VECTASHIELD (Vector Laboratories) and analyzed using a Nikon A1R Confocal Microscope at 60X. Intensity of phospho-53BP1-GLI1-UBF1 co-localization was determined using the manufacturer's protocol for calculating binary intersection mean intensity in NIS-Elements (Nikon) software from five random confocal images.

Nucleolar isolation

Nucleoli were purified using a published protocol (18) with minor adaptation. Cells were plated onto 100 mm tissue culture dishes in complete media. After reaching 90% confluence, they were washed three times with cold PBS at pH 7.4 and were collected in a minimal volume of PBS using cell scraper. Pooled cells from at least 10 dishes were centrifuged at 500 *g* for 5 min. The Reference Volume (RV) was then determined by visually estimating the volume of the cell pellet. Cell pellets were resuspended in 15 RV of Nucleoli Standard Buffer (NSB) (10 mM Tris–HCl, pH 7.4, 10 mM NaCl, 1 mM $MgCl_2$ and HALT protease and phosphatase inhibitor cocktail) and incubated on ice for 30 min. NP-40 (Roche) was then added to a final concentration of 0.3%. The cells were homogenized using a 7 ml Dounce homogenizer (Wheaton). The homogenate was centrifuged at 1200 *g* for 10 min. The supernatant containing the cytoplasmic fraction was removed and the pellet was resuspended in 10 RV of 250 mM sucrose containing 10 mM $MgCl_2$. Nuclei were then purified from the homogenate by centrifugation at 1200 *g* for 10 min through an 880 mM sucrose cushion containing 5 mM $MgCl_2$. Purified nuclei were resuspended in 10 RV of 340 mM sucrose containing 5 mM $MgCl_2$ and sonicated using several 10-s pulses with 60-s rests on ice between pulses. Membrane disruption was confirmed with phase contrast microscopy to ensure the absence of intact cells and that the nucleoli were devoid of their surrounding nuclei. Nucleoli were then purified from the homogenate by centrifugation at 2000 *g* for 20 min at 4°C through an 880 mM sucrose cushion containing 5 mM $MgCl_2$. Purified nucleoli were resuspended in 340 mM sucrose containing the HALT inhibitor cocktail and stored at −80°C for later analysis.

Luciferase reporter assay

Cells were counted by hemocytometer and plated at 25 000 cells per well in a 96-well plate (Corning). After 24 h, each well was transfected with 50 ng of 8XGli-BS-Luc reporter plasmid (19) using FuGENE 6 (Promega). Twenty-four hours after transfection, they were irradiated with 4 Gy as noted. The experiment was terminated 6 h later for measuring luciferase activity using the Luciferase Assay System (Promega) and a GloMax 20/20 Luminometer (Promega) according to manufacturer's protocol. Experiments were performed in triplicate and normalized to total protein content as measured by Precision Red assay.

Endogenous protein co-immunoprecipitation

SUM1315 cells were raised to confluence and treated as indicated. At the listed times, cells were washed in ice cold PBS and lysed in RIPA buffer containing HALT protease and phosphatase inhibitor cocktail. Lysates were kept on ice for 1 h before being syringe-passed 15 times through a 21 G needle and clarified by centrifugation at 10 000 RPM for 10 min at 4°C. Protein concentration was measured by Precision Red and equal amounts of lysate (750 μg) were used for each immunoprecipitation and corresponding non-specific binding control, with 30 μg of whole cell lysate set aside as an input loading control. Lysates were incubated and rotated with or without α-GLI1 (Cell Signaling, 2643S) for 16 h at 4°C before being added to 30 μL slurry of Protein A/G PLUS-Agarose beads (Santa Cruz, sc-2003) washed in PBS prior to use. After 4 h of rotation at 4°C, beads were isolated by centrifugation and washed in RIPA buffer three times before immunoprecipitated protein was released by adding denaturing sample buffer containing fresh β-mercaptoethanol and boiled at 95°C for 5 min. Immunoblotting for GLI1 in this experiment was done with an antibody from a different source animal (Cell Signaling, 2553S) to avoid detection of potentially confounding IgG peptides.

RNA isolation

Cells were washed in ice cold PBS before RNA was harvested using the PureLink RNA Mini Kit (Ambion) according to manufacturer instructions. Quality of RNA was confirmed by A260:280 ratio and quantitated using the NanoDrop Lite spectrophotometer (Thermo Fisher).

Quantitative PCR

When appropriate, cDNA was reverse transcribed from equal amounts (1 μg) of isolated RNA using the High Capacity Reverse Transcription Kit (Applied Biosystems). Quantitative PCR was done using the Step ONE Plus Real Time PCR System (Applied Biosystems) with either TaqMan Fast Advanced Master Mix (Applied Biosystems) or Maxima SYBR Green/ROX qPCR Master Mix (Thermo Scientific). TaqMan primers (LifeTech) used were GLI1 (Hs01110766_m1) and ACTB (Hs99999903_m1). Primers used for SYBR Green reactions are tabulated in Supplementary Table S1. For RNA polymerase I activity assays, cDNA was diluted 1:50 prior to use. All reactions were done in triplicate and expression relative to stated controls was calculated using the $\Delta\Delta C_T$ method unless otherwise noted.

Neutral comet assay

Neutral comet assays were done using the CometAssay Kit (Trevigen) according to manufacturer's protocol. Following staining with SYBR Gold (Invitrogen), 50 cells per slide well were analyzed using Comet Assay IV software (Instem).

GFP-based NHEJ repair assay

The reporter plasmid and assay have been previously described (20). SUM1315 and MDA-MB-468 cells were transfected with the pimEJ5-GFP reporter plasmid using Lipofectamine 2000 (Invitrogen) according to manufacturer's protocol and maintained in selection with 2 μg/ml puromycin (Sigma) for 4 weeks before resistant colonies were isolated and further expanded. 80 000 stably transfected cells were then seeded per well in a 12-well plate (Corning) in triplicate. After 24 h, each well was transfected with 2 μg of I-SceI plasmid using FuGENE 6 according to manufacturer's protocol. Parallel transfection of GFP was done to estimate transfection efficiency. Media was replaced with the appropriate complete media containing either DMSO or 10 μM GANT61. Prior to harvest, cells were stained with 7-aminoactinomycin D (Invitrogen) as a viability control. Flow cytometry was done to quantify the percentage of GFP-expressing cells 72 h after transfection, with 100 000 events collected per sample. Data were analyzed using FlowJo (Tree Star).

Luciferase-based NHEJ reporter assay

The reporter assay has been previously described (20,21). pGL3-Control (Promega) plasmid was digested with HindIIII (Thermo Scientific) to create a double-strand break between the promoter and firefly luciferase coding sequence. Digested plasmid was then treated with calf intestinal phosphatase (Thermo Scientific) to mitigate spontaneous re-ligation. Linearized plasmid was confirmed by electrophoresis and isolated using the Monarch DNA Gel Extraction Kit (New England Biolabs). Cells were plated at a density of 25 000 per well in a 96-well plate. After 24 h, each well was transfected with 50 ng of either linearized or uncut plasmid as well as 10 pg of Renilla luciferase vector as a transfection efficiency control using FuGENE 6. Luciferase activity was measured 24 h after transfection using the Dual Luciferase Reporter Assay System (Promega) and normalized to the Renilla luciferase signal. Data are reported as a percentage of the normalized firefly luciferase activity from cells transfected with uncut pGL3-Control plasmid. All assays were done in triplicate.

RNA polymerase (Pol) I activity assay

The activity assay has been previously described (22). RNA Pol I activity was determined by using quantitative PCR to measure expression of two amplicons within the short-lived 5′ external transcribed spacer (ETS) region of the 47S pre-rRNA (Supplementary Table S1). RNA was isolated and used to generate cDNA as described above. cDNA was diluted 1:50 prior to quantitative PCR as described above.

I-PpoI cleavage assay

Cells were transfected with pBABe-HA-ER-IPpoI (23) using FuGENE6 according to manufacturer's protocol. Sixteen hours after transfection, cells were plated in 35 mm dishes and subsequently treated with 1 μM tamoxifen (Sigma) or ethanol vehicle control as noted. Sixteen hours after initiating treatment, tamoxifen-containing media was replaced with complete media. Genomic DNA was isolated at the indicated time-points after tamoxifen withdrawal using the QIAamp DNA Mini Kit (Qiagen) and assessed for I-PpoI induced damage at 45S rDNA loci using quantitative PCR to measure an amplicon spanning the restriction site (Supplementary Table S1), such that unrepaired breaks would reduce expression. 5 ng of genomic DNA was used for each reaction, which were done in triplicate and normalized to β-actin expression.

Three-dimensional (3D) culture

SUM1315 and MDA-MB-468 cells were pre-treated with GANT61 for 24 hours and irradiated with 4 Gy. 200 μl of Cultrex 3D Culture Matrix Reduced Growth Factor Basement Membrane Extract (RGF BME) was added to a sterile eight-well chamber (Millipore) and allowed to solidify at 37°C for 30 min. Cells were trypsinized, counted by hemocytometer, and diluted in assay medium before seeding to a final density of 5000 cells per well containing the 3D matrix. Assay medium was replaced every 4 days. Cell growth was captured and analyzed on day 8 and day 16 for SUM1315 and MDA-MB-468 cells, respectively. A Nikon Eclipse TE2000-U microscope was used to visualize cells at 30× magnification. ImageJ software was used to measure spheroids.

Colony formation assays

SUM1315 cells were treated for 24 h with either DMSO or 20 μM GANT61. Cells were then mock irradiated or irradiated with 4 Gy as indicated. Four hours after irradiation, plates were washed with PBS and cells were trypsinized for counting by hemocytometer. Cells were seeded in triplicate in six-well plates (Corning) at a density of 1500 cells per well in either DMSO- or GANT61-containing medium. Twenty-four hours after seeding, media was gently aspirated and replaced with complete medium without drug. Alternatively, SUM1315 cells stably transfected with non-targeting shRNA or shGLI1 were irradiated and seeded as noted in complete medium containing G418 without replacement of media after plating. Ten days after seeding, plates were washed with PBS and cells were fixed using 4% PFA before staining with 0.1% crystal violet (Sigma) in 10% ethanol (Pharmco) for counting.

I-PpoI colony formation assay

SUM1315 non-targeting (NT) or shGLI1 were transfected with pICE-HA-NLS-I-PpoI or empty vector using Fugene 6 as per manufacturer protocol. Briefly, cells were transfected in 60 mm dishes, and 48 hours post transfection cells were seeded at low density in six-well plates. Colonies were allowed to form 7–10 days post seeding. Foci were stained with 0.1% crystal violet and were counted using ImageJ analysis software. All experiments were done in triplicate and represented as percent change of I-PpoI versus vector control. Statistical analysis was performed using a One-Way ANOVA and p values are indicated. pICE-HA-NLS-I-PpoI was a gift from Steve Jackson (Addgene plasmid # 46963; http://n2t.net/addgene:46963; RRID:Addgene_46963).

MTS assay

SUM1315 cells stably transfected with non-targeting (NT) shRNA or shGLI1 were seeded in a 96-well plate at a density of 5000 cells per well in either plain media or (0.1, 0.5, 1, 2.5, 5, 7.5, 10) μM doxorubicin-containing media for 48 h. Plates were replenished with medium containing MTS reagent (Promega), incubated for 1hr, and absorbance was recorded at 490 nm for colorimetric determination of viable cells.

Statistics

Prism 8 (GraphPad) was used for data visualization and statistical analyses. Results shown are representative examples from at least three independent replicates. All error bars shown represent the standard error of the mean. Statistical significance was defined as $P < 0.05$. Details about specific tests applied are in the respective legends. Unless otherwise noted below, statistics were calculated from $n = 3$ technical replicates from an individual experiment. For neutral comet assays, $n = 50$ cells were counted per condition. For γ-H2AX foci and phospho-53BP1 foci, n was dependent on the number of cells counted in 10 random 30× fields. For 3D cultures, $n = 50$ spheroids per condition were counted.

RESULTS

GLI1 localizes to 45S rDNA repeats in response to IR

To explore the hypothesis that DNA damage induces cistromic changes in GLI1, we undertook an unbiased screening approach in SUM1315 triple-negative breast cancer (TNBC) cells known to have aberrant activation of Hh signaling reflected by high endogenous levels of GLI1. GLI1-associated chromatin was immunoprecipitated from cells four hours after 4 Gy IR or mock irradiation (Supplementary Figure S1A) and evaluated by next-generation sequencing (ChIP-Seq). We found that GLI1 associates with a novel motif (Figure 1A and Supplementary Figure S1B) that is distinct from the previously reported core sequence (5′-GACCACCCA-3′) (24). We identified ChIP-Seq peaks that were specific to the irradiated and nonirradiated samples (Supplementary Tables S2 and S3). Surprisingly, unique peaks specific to irradiated cells were markedly enriched for rDNA loci, with approximately a third of the hits associated with RNA5S1–17, RNA45SN1–5, RNA18SN1–5, RNA28SN1–5 and RNA5–8SN1–5 (Figure 1B). We manually searched the 45S rDNA coding sequence for putative GLI1 interacting sequences based either on the previously reported core sequence or the motif calculated from our ChIP-Seq data. Using the Integrated Genomics Viewer (17) to visualize peaks at these potential sites, we focused on five putative GLI1 binding sites with associated peaks that were enhanced after irradiation, ruling out candidates where no peak was seen (Figure 1C). Site A is based on the previously reported consensus and is located in the 5′ external transcribed spacer (ETS). Sites B–E are based on our novel predicted binding sequence and cluster in the 28S region. To validate results of the ChIP-Seq screen, we performed quantitative PCR of immunoprecipitated chromatin and discovered that GLI1 association with these five sites was induced as early as 1 hour following 4 Gy IR (Figure 1D). Because the 45S rDNA repeats comprise the nucleolar organizer regions (NORs), we enriched nucleoli through a sucrose cushion and found that the nucleolar fraction of GLI1 is increased in response to IR (Supplementary Figure S1C). Using immunocytochemistry, we were able to visualize nucleolar GLI1 in irradiated cells. The incidence (Figure 1E) and intensity (Figure 1F) of nucleolar GLI1 as evidenced by its colocalization with fibrillarin was significantly elevated in SUM1315 cells following IR compared to non-irradiated controls.

Hh activity is induced by IR and facilitates resolution of DSBs

We observed a significant increase in GLI1 reporter activity in response to IR as evidenced in three different TNBC cell lines (Figure 2A), suggesting an increase in Hh activity. Concordantly, we registered a significant increase in transcript (Figure 2B) and a concurrent qualitative rise in protein levels (Figure 2C) of GLI1 in irradiated SUM1315 and MDA-MB-468 cells. This is also evident when cells are irradiated with low-dose IR (Supplementary Figures S2A, B). Abrogating GLI1 expression (shGLI1) did not induce appreciable dsDNA damage (Supplementary Figure S2A). Furthermore, even when low dose IR is used to induce DNA damage, cells silenced for GLI1 sustained significantly increased dsDNA damage (Supplementary Figures S2A, B). To better understand the relevance of IR-induced Hh activation, we inhibited the activity of GLI using GANT61, a direct GLI1/2 inhibitor (Figure 2D, E). This resulted in persistence of IR-induced γ-H2AX expression, suggesting delays in DNA repair (Figure 2E). Complementing the outcomes of SUM1315 cells, MDA-MB-468 cells inhibited for Hh/GLI signaling also demonstrated persistence of IR-induced γ-H2AX expression, although the kinetics between these two cell systems was markedly distinct. (Figure 2E and Supplementary Figure S2C). Hh inhibition using the SMO inhibitor vismodegib (Supplementary Figures S2D and S2E) or stable transfection of GLI1-targeting shRNA (shGLI1) yielded similar findings (Supplementary Figure S2F). This corresponded with statistically significant delays in resolution of IR-induced γ-H2AX foci visualized using immunocytochemistry (Figure 2F). To more specifically examine DSBs, we used neutral comet assays to measure average tail moments in SUM1315 and MDA-MB-468 cells pretreated with GANT61 and then exposed to 4 Gy IR (Figure 2G). As anticipated, the average tail moment increased in irradiated cells with evidence of resolution over time in vehicle-treated cells. However, GANT61-pretreated cells were unable to recover. Hh inhibition using stable transfection of shGLI1 yielded similar results compared to non-targeting shRNA control (Supplementary Figure S2G). Collectively, these findings suggest that inhibiting Hh signaling delays IR-induced DSB repair.

Hh signaling is required for efficient NHEJ

Recalling our initial finding that GLI1 is enriched at rDNA loci following IR, we conjectured that GLI1 pro-

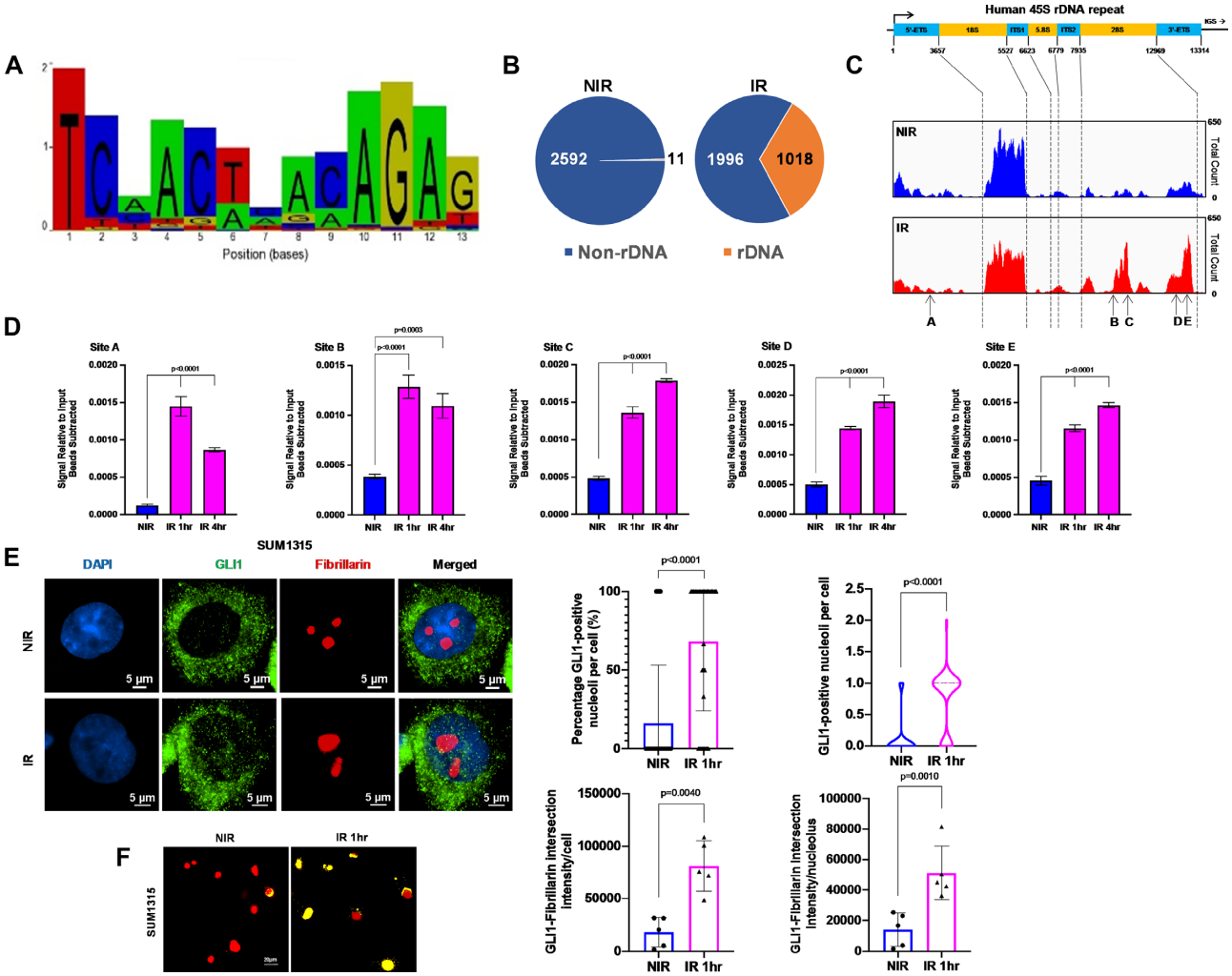

Figure 1. Ionizing radiation induces GLI1 binding to novel sequences in rDNA. (**A**) ChIP-Seq data was used to predict a novel GLI1-associated sequence after IR. (**B**) Unique ChIP-Seq peaks following IR were enriched in rDNA loci compared to NIR. (**C**) GLI1 association was increased in the 28S region of 45S rDNA after IR at sites A-E. (**D**) Five putative GLI1 binding sites (A–E) show increase in GLI1 occupancy after IR and were validated with ChIP-qPCR. Statistical significance was determined with a one-way ANOVA and Dunnett's multiple comparison test, comparisons between NIR- and IR-treated cells are shown. (**E**) Immunocytochemistry demonstrates higher GLI1 presence in the fibrillarin-positive nucleoli 1hr after IR, quantitated as a percentage of nucleoli per cell or absolute number of nucleoli. (**F**) Fibrillarin and GLI1 co-localization, depicted in yellow, increases after IR, normalized either to the total number of cells or nucleoli using NIS binary intersection mean intensity ($n = 5$). Significance was determined by using t-test. All error bars depict the SEM.

motes rDNA repair, which preferentially utilizes NHEJ (9). SUM1315 and MDA-MB-468 cells were stably transfected with the pimEJ5-GFP reporter plasmid, a construct used to assay NHEJ activity. After site-specific DSBs were induced by the restriction enzyme I-SceI (Supplementary Figure S3A), GFP-expressing cells that had undergone successful NHEJ-mediated repair were quantified by flow cytometry. Hh inhibition by GANT61 significantly impaired NHEJ in both cell lines (Figure 3A). In an independent verification, we linearized pGL3-Control with the restriction enzyme HindIII, disconnecting the promoter from the firefly luciferase coding sequence. Cells transfected with HindIII-cut pGL3-Control will only express firefly luciferase if NHEJ has resolved the break. Again, GANT61 significantly reduced NHEJ-mediated repair (Figure 3B). We also assessed the possible role of HR in IR-induced dsDNA damage using the DR-GFP luciferase reporter construct. While BRCA1-mutated SUM1315 cells demonstrated a smaller magnitude of HR activity, this was unchanged in presence of GANT61. In MDA-MB-468 cells, GANT61 reduced HR-mediated repair, albeit the overall magnitude of HR activity was very small (Supplementary Figures S3B, C).

Prior work has suggested that GLI1 may interact with the DSB-sensing proteins MRE11 and RAD50 (25). Using endogenous protein co-immunoprecipitation, we found that GLI1 interacts with 53BP1, a protein critical for dictating repair pathway choice towards NHEJ (26) (Figure 3C).

The interaction of endogenous GLI1 with 53BP1 is accompanied by active *P*-53BP1 foci at DSB sites (Figure 3D, E). This suggests that the interaction between GLI1 and 53BP1 is likely important for the rapid NHEJ repair response and *P*-53BP1 foci formation at DSB sites.

Furthermore, IR-induced expression of *P*-53BP1 and abundance of *P*-53BP1 foci were reduced when Hh was in-

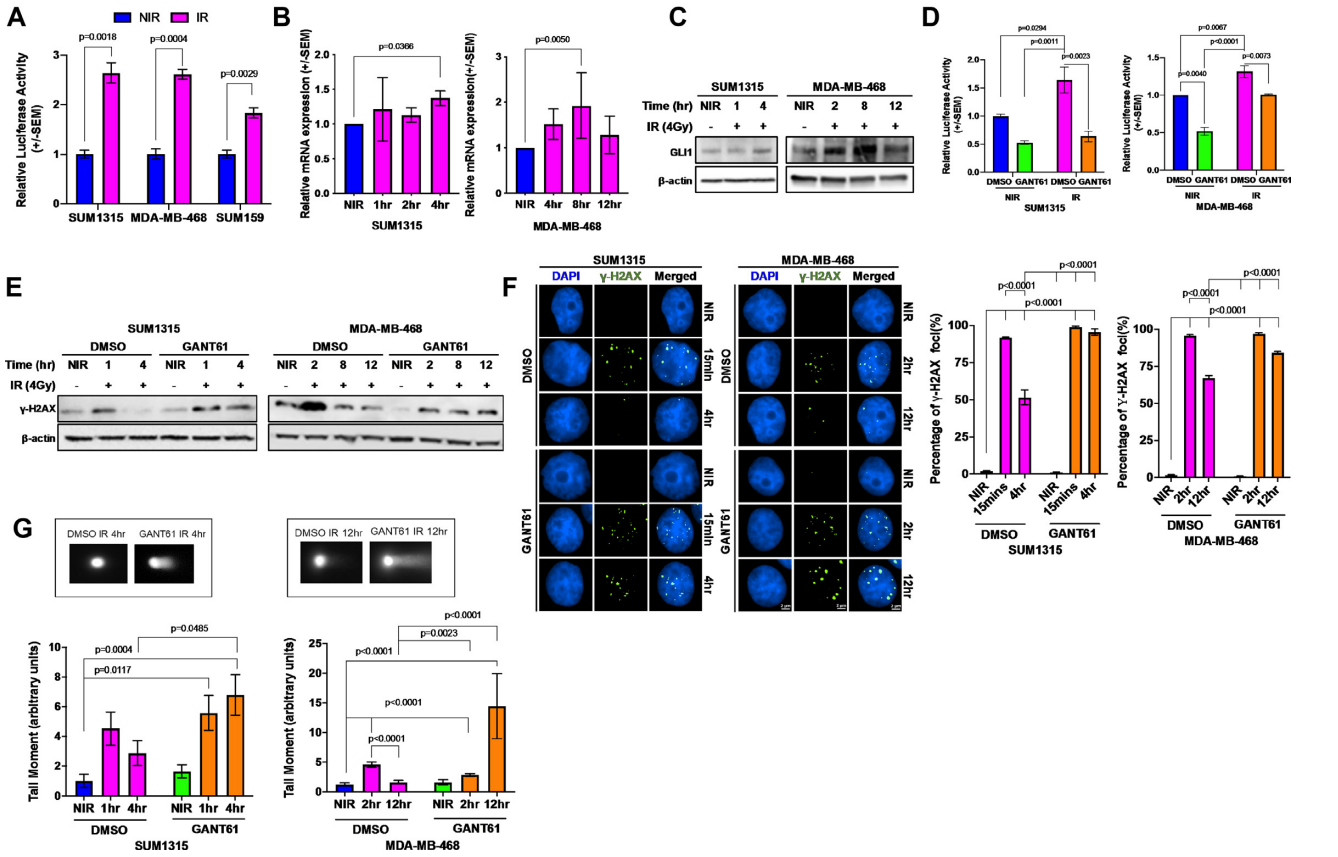

Figure 2. Inhibition of Hh/GLI signaling delays ionizing radiation-induced DSB repair in TNBC cells. (**A**) 8X-GBS-luciferase reporter assays show Hh activation in multiple TNBC cell lines after IR, confirmed by GLI1 (**B**) mRNA and (**C**) protein expression using qPCR and immunoblotting, respectively in SUM1315 and MDA-MB-468 cell lines. Statistical significance was determined with a multiple t test and a one-way ANOVA with Dunnett's multiple comparison test. For one-way ANOVA, comparisons between NIR- and IR-treated cells are shown. (**D**) GANT61 suppresses IR-induced Hh activation. Statistical significance represents the results of a two-way ANOVA and Tukey multiple comparison test. (**E**) GANT61 leads to delayed resolution of IR-induced γ-H2AX after IR shown by immunoblot compared to vehicle control. (**F**) IR-induced γ-H2AX foci shown by immunocytochemistry show similar delay in foci resolution. (**G**) Neutral comet assays show impaired DSB repair in GANT61-treated cells. Statistical significance was determined with a two-way ANOVA and Tukey's multiple comparison test. Comparisons for DMSO treated NIR and DMSO treated IR-4 h for SUM1315 and IR-12 h for MDA-MB468 are shown. All error bars depict the SEM.

hibited by either GANT61 (Figure 3D) or GLI1 knockdown (Figure 3E, Supplementary Figures S3D, E).

Hh signaling is required for resolution of site-specific rDNA DSBs

Because these assays address global DNA repair, we sought to assess how rDNA repair specifically is affected by Hh inhibition. To do so, we transfected cells with tamoxifen-inducible I-PpoI (pBABe-HA-ER-IPpoI), a restriction enzyme with limited recognition sites in the human genome, including one in the 45S rDNA sequence (Supplementary Figure S3F). Due to the sheer number of 45S rDNA repeats found throughout the human genome, I-PpoI-induced DNA breaks can be considered a surrogate for rDNA-specific damage (23). We first confirmed that tamoxifen treatment of cells transfected with pBABe-HA-ER-IPpoI reduced abundance of an amplicon spanning the I-PpoI cleavage site in the 45S rDNA sequence by qPCR, indicating breakage (Supplementary Figure S3G). Concomitant with this, we also registered phosphorylation of NBS1 and ATM, which are previously reported indicators of I-PpoI-mediated damage (Supplementary Figure S3H) (23). Using ChIP, we found that GLI1 localizes to the sites of I-PpoI-mediated breaks in 45S rDNA (Figure 3F). To evaluate the role of GLI1 in the resolution of these breaks, we withdrew tamoxifen after overnight treatment to allow for repair. The abundance of an amplicon spanning the I-PpoI restriction site was reduced by tamoxifen treatment, indicating the presence of breaks that the polymerase was unable to read through (Figure 3G). After tamoxifen was withdrawn for four hours, the magnitude of amplicon abundance increased again in control (NT) cells, implying repair of the cleavage site. We found that GLI1 knockdown (shGLI1) significantly hampered the recovery of amplicon expression after tamoxifen withdrawal, suggesting that GLI1 is required for the efficient repair of site-specific rDNA DSBs. Resolution of rDNA breaks requires the recruitment of repair machinery to sites of damage. Using confocal microscopy, we observed the colocalization of GLI1 and *P*-53BP1 in the nucleolus in response to IR (Figure 3H and Supplementary Figure S3I). We quantified the intersection

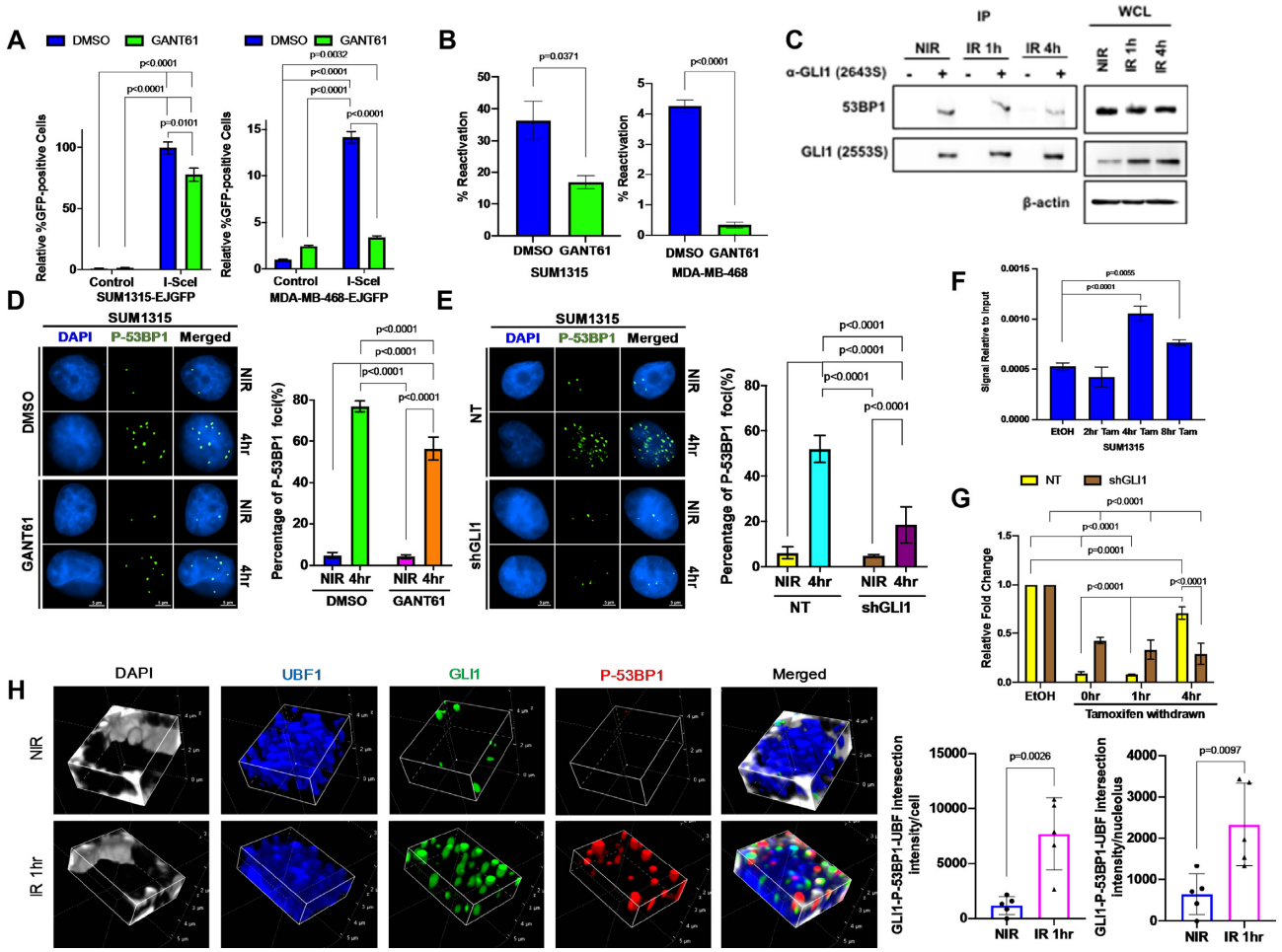

Figure 3. Hh inhibition impairs NHEJ and delays repair of rDNA DSBs. (**A**) Hh inhibition compromises repair of I-SceI-induced breaks by NHEJ in cells stably expressing the pimEJ5-GFP reporter. Statistical analysis was performed with a two-way ANOVA and Tukey's multiple comparison test, p values are indicated. (**B**) Impaired NHEJ in Hh-inhibited cells is also evident by diminished reactivation of linearized firefly luciferase plasmid. Statistical analysis was determined with a *t*-test. (**C**) Endogenous protein co-immunoprecipitation of SUM1315 lysates shows that 53BP1 interacts with GLI1. Whole cell lysate (WCL) input controls are shown to the right. (D, E) *P*-53BP1 foci are reduced by (**D**) GANT61 and (**E**) stable knockdown of GLI1 compared to controls in SUM1315 cell line at 4 h post-IR. Statistical analysis was performed with a two-way ANOVA and Tukey's multiple comparison test, p values are indicated. (**F**) GLI1 localizes to I-PpoI-induced rDNA breaks as evidenced by greater occupancy at the I-PpoI break-site following tamoxifen treatment shown by ChIP-qPCR. Statistical significance was determined with a a one-way ANOVA and Dunnett's multiple comparison test, comparisons between ethanol treated and tamoxifen withdrawn cells are shown. (**G**) Tamoxifen treatment induces breaks in SUM1315 NT and shGLI1 cells as measured by reduction in magnitude of amplicon spanning the I-PpoI restriction site. 4 hr post tamoxifen withdrawal, amplicon levels in NT cells increase but stable knockdown of GLI1 remains unchanged indicating efficient repair of these sites of damage in NT compared to shGLI1. Statistical significance was determined with a two-way ANOVA and Tukey's multiple comparison test for treatment at respective time points. Comparisons for ethanol-treated and tamoxifen withdrawn cells and comparison at 4 h after tamoxifen withdrawal between NT and shGLI1 cells are shown. (**H**) 3D confocal images of NIR (top) and IR (bottom) SUM1315 cells labeled with GLI1 (green), *P*-53BP1 (red), UBF (blue), and DAPI (gray) depict increased nucleolar localization and interaction of GLI1 and *P*-53BP1 1 h post IR in the nucleolar compartment. GLI1 and *P*-53BP1 interaction in the nucleolus was quantified from five NIR and IR cells and normalized either to the number of cells or nucleoli per field using NIS binary intersection mean intensity ($n = 5$). All error bars depict the SEM.

of GLI1, *P*-53BP1, and the nucleolar marker UBF1 at one-hour post-irradiation and noted a substantial increase in their association per cell and per nucleolus (Figure 3H).

Combining Hh inhibition with IR compromises Pol I activity and cell viability

rDNA DSBs temporarily arrest transcription until repair is complete. To assess how Hh inhibition affects 45S rDNA transcription by Pol I in response to damage, we used qPCR to quantify expression of two different sites in the 5′ ETS. Because these regions are removed post-transcriptionally during rRNA processing, they have a short half-life and are ideal surrogates for Pol I activity over time (22). As anticipated, in control cells treated with vehicle, Pol I activity was reduced early in response to IR and recovered at later time points (Figure 4A and B), consistent with the kinetics of repair determined by our earlier experiments. When Hh activity was inhibited by GANT61, Pol I activity is reduced by IR as expected, but does not recover. Hh inhibition by stable GLI1 knockdown yielded similar results (Supplementary Figures S4A and S4B). Interestingly, the delay in Pol I recovery that we observed with GLI1 inhibition mirrors prior findings when NHEJ was directly inhibited instead

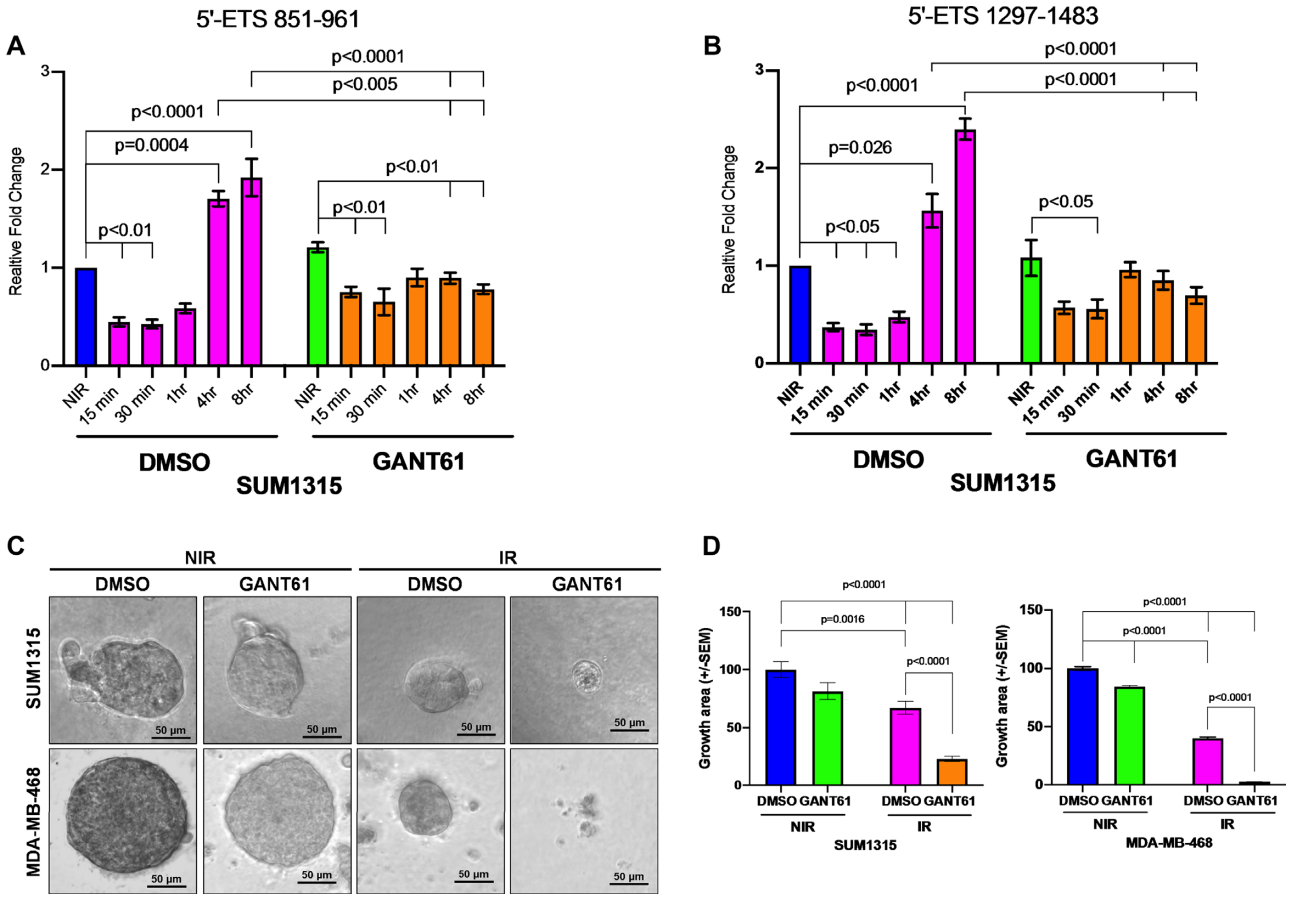

Figure 4. Inhibiting Hh/GLI signaling impairs re-activation of Pol I activity following irradiation-induced DSBs. (**A, B**) Pol I activity, as quantitated by qPCR of two different amplicons in the 5' ETS of 45S rDNA, is reduced by IR and recovers following repair in cells treated with vehicle control compared to GANT61-treated cells. Statistical significance was determined with a two-way ANOVA and Tukey's multiple comparison test. Comparisons for DMSO- and GANT61- NIR group with cells collected at different time points post IR and DMSO- and GANT61-treated cells at 4 and 8 h are shown. (**C, D**) Hh inhibition with GANT61 combined with IR almost completely abrogates spheroid growth, compared to more modest reductions with either modality alone. Growth area was quantified using ImageJ software per 10× field. Statistical significance was determined with a two-way ANOVA and Tukey's multiple comparison test for each condition. All error bars depict the SEM.

(9). We then explored whether Hh pathway inhibition would lead to sensitivity due to its role in rDNA repair. In order to specifically induce rDNA breaks, we transfected SUM1315 cells with I-PpoI plasmid or an empty vector control. In order to specifically address the role of Hh/GLI activity, we queried SUM1315 cells stably silenced for GLI1. We assessed the effect on cell survival using a colony formation assay. Introducing I-PpoI caused an appreciable decrease in the number of colonies relative to control plasmid (Supplementary Figure S4C, D). Interestingly, GLI1-silenced cells transfected with I-PpoI showed a striking decrease in the number of colonies formed, suggesting that Hh inhibition further reduces survival of cells inflicted with rDNA breaks with I-PpoI. These findings support that Hh inhibition augments rDNA damage and consequently poses finite lethality to TNBC cells independent of global effects on DSB repair.

To assess the overall outcome of IR-induced DNA damage in the context of Hh inhibition, we generated spheroids in three-dimensional culture from cells pre-treated with either vehicle control or GANT61 (Figure 4C and D). GANT61 alone had a modest effect on non-irradiated cells, but dramatically impaired spheroid growth when combined with irradiation in both SUM1315 and MDA-MB-468 cells. Similar findings were noted with GLI1 knockdown (Supplementary Figure S4E). Similarly, colony formation, following irradiation, was significantly compromised in cells deficient for Hh/GLI activity (Supplementary Figures S4F and G). Next, we examined whether Hh activity also impacts survival of breast tumor cells when DNA damage is inflicted with the anthracycline doxorubicin, a topoisomerase inhibitor that generates DSBs. We scored cell survival with a colony formation assay using doxorubicin in lieu of IR, and saw that doxorubicin (used at 0.1 μM) significantly compromised the abundance of colonies formed by GLI1-deficient SUM1315 cells compared to NT shRNA controls (Supplementary Figures S4H and I). We also scored cell viability using the MTS assay and registered a significant decrease in cell viability in doxorubicin-treated SUM1315 shGLI1 cells relative to NT cells ($P < 0.01$) (Supplementary Figure S4J). As such, the data cumulatively indicates that Hh inhibition sensitizes TNBC cells to IR and doxorubicin, both of which are clinically relevant agents used to treat TNBC.

DISCUSSION

Hh signaling is a classical developmental pathway that is aberrantly activated in various cancers (27) and has been linked to tumor initiation, progression and metastasis in breast cancer. In TNBC patients, high expression of Hh pathway proteins correlates to poor survival (28,29). Treatment of TNBC relies on DNA-damaging agents, including conventional chemotherapy and IR (30). Though inhibiting Hh has been shown to sensitize cancer cells to genotoxic therapies, the underlying mechanisms to this point have remained vague (12,13). Our study has uncovered an unexpected role for Hh signaling in the repair of damaged rDNA that helps to explain this phenomenon.

Though we found that GLI1 is required for efficient NHEJ-mediated repair of nonspecific DSBs, we demonstrated a marked enrichment of GLI1 at rDNA loci in response to IR using an unbiased ChIP-Seq screen and confirmed this relative to nonspecific binding controls with standard ChIP. Importantly, the precise degree of enrichment at rDNA loci relative to standard genes is unclear. rDNA coding sequences are known to be arranged in tandem arrays of tens to hundreds of repeats, but only 17 5S rDNA sequences and five 45S rDNA sequences are mapped to the current build of the human genome. This was recently identified as a critical unmet need in the rDNA field (31). For this reason, we focused on the defined coding sequences and not the poorly defined intergenic spacers between repeats. Though we found more hits were associated with 5S rDNA repeats, we elected to study the 45S rDNA both because of the availability of tools to study its gene expression (qPCR of the 5′-ETS) and site-specific DSBs (I-PpoI) and because 45S rDNA breaks have been previously shown to be more consequential than those in 5S rDNA (5). Even accounting for the likelihood that pulled-down fragments mapped to multiple repeats, our findings may underestimate the degree of GLI1 interaction with rDNA given the vast number of repeats known to exist in the human genome.

Notably, we did not observe similar enrichment of GLI1 at genes associated with NHEJ, including *XRCC5*, *XRCC6*, *PRKDC*, *LIG4* and *TP53BP1*, which encode for Ku70, Ku80, DNA-PKcs, DNA ligase IV, and 53BP1, respectively. This suggests that the effect of GLI1 on NHEJ is not related to its transcription factor activity, despite our finding that GLI1 expression and activity are increased in response to IR. Whether the enrichment of GLI1 at rDNA loci is influenced by upregulated GLI1 protein expression or shifts in subcellular localization that we observed in response to IR remains an open question.

Accordingly, we hypothesized that GLI1 instead recruits NHEJ-associated proteins to the sites of rDNA DSBs. In line with this conjecture, we found that GLI1 interacts with the NHEJ protein 53BP1. Furthermore, we observed using confocal microscopy that GLI1 association with both *P*-53BP1 and the rDNA marker UBF1 is triggered by IR. Inhibition of GLI1 mutes the accumulation of *P*-53BP1, interferes with repair of site-specific rDNA DSBs, and delays recovery of Pol I activity, an indicator of unrepaired rDNA DSBs, in response to IR. To our knowledge, this is the first example of a developmental signaling pathway being directly tied to rDNA repair. Given that Hh signaling is intimately involved in orchestrating normal ontogeny and cancer, it is likely that dysregulated Hh activity may craft intersecting and shared programs that enable cells to survive erroneous and possibly lethal impediments.

Interestingly, inhibiting Hh did not impair baseline Pol I activity on its own. Instead, its effect is secondary to compromised rDNA repair. Thus, GLI1 does not appear to directly promote rRNA transcription, but rather helps to maintain the genomic integrity of rDNA loci. These sites may be particularly vulnerable in proliferative and metabolically active states where Hh is activated, such as in normal development and cancer. In this context, protecting rDNA loci from insults such as replication stress and DNA-damaging agents may be a critical new function of Hh signaling with potential implications for therapeutic resistance in cancer. Our findings suggest that further evaluation of Hh inhibitors as potential radiosensitizers or chemosensitizers is warranted.

DATA AVAILABILITY

The datasets used and/or analyzed during the current study have been deposited at the Gene Expression Omnibus (GEO) under the accession number GSE146237.

SUPPLEMENTARY DATA

Supplementary Data are available at NAR Online.

ACKNOWLEDGEMENTS

We thank the UAB Animal Resources Program for the use of irradiator facilities; the UAB Comprehensive Flow Cytometry Core for the use of flow cytometry facilities; the UAB High Resolution Imaging Facility and Dr R. Grabski for technical assistance; J.M. Stark for providing the pimEJ5-GFP construct via AddGene; M.B. Kastan for providing the pBABe-HA-ER-IPpoI construct via AddGene; J.A. Bonner for the use of comet analysis facilities and H.Q. Trummell for related technical assistance and guidance; and E.S. Yang for providing the I-SceI construct and technical expertise.

FUNDING

NCI/NIH [CA183926 to V.T.G.L.]; Merit Review Award [I01 BX003374] from the U.S. Department of Veterans Affairs BLRD service BX003374; NCI/NIH [CA194048 to R.S.S., CA169202 to L.A.S.]; United States Department of Defense [W81XWH-18-1-0036 to L.A.S.]; University of Alabama at Birmingham [AMC21 to L.A.S.]; Breast Cancer Research Foundation of Alabama [to L.A.S.]. Funding for open access charge: Institutional start-up funds.
Conflict of interest statement. None declared.

REFERENCES

1. Pelletier,J., Thomas,G. and Volarevic,S. (2018) Ribosome biogenesis in cancer: new players and therapeutic avenues. *Nat. Rev. Cancer*, **18**, 51–63.

2. Tchurikov,N.A., Fedoseeva,D.M., Sosin,D.V., Snezhkina,A.V., Melnikova,N.V., Kudryavtseva,A.V., Kravatsky,Y.V. and Kretova,O.V. (2015) Hot spots of DNA double-strand breaks and genomic contacts of human rDNA units are involved in epigenetic regulation. *J. Mol. Cell Biol.*, **7**, 366–382.
3. Tchurikov,N.A., Yudkin,D.V., Gorbacheva,M.A., Kulemzina,A.I., Grischenko,I.V., Fedoseeva,D.M., Sosin,D.V., Kravatsky,Y.V. and Kretova,O.V. (2016) Hot spots of DNA double-strand breaks in human rDNA units are produced in vivo. *Sci. Rep.*, **6**, 25866.
4. Stults,D.M., Killen,M.W., Williamson,E.P., Hourigan,J.S., Vargas,H.D., Arnold,S.M., Moscow,J.A. and Pierce,A.J. (2009) Human rRNA gene clusters are recombinational hotspots in cancer. *Cancer Res.*, **69**, 9096–9104.
5. Warmerdam,D.O., van den Berg,J. and Medema,R.H. (2016) Breaks in the 45S rDNA lead to Recombination-Mediated loss of repeats. *Cell Rep.*, **14**, 2519–2527.
6. Roukos,V. and Misteli,T. (2014) The biogenesis of chromosome translocations. *Nat. Cell Biol.*, **16**, 293–300.
7. Ceccaldi,R., Rondinelli,B. and D'Andrea,A.D. (2016) Repair pathway choices and consequences at the double-strand break. *Trends Cell Biol.*, **26**, 52–64.
8. Scully,R., Panday,A., Elango,R. and Willis,N.A. (2019) DNA double-strand break repair-pathway choice in somatic mammalian cells. *Nat. Rev. Mol. Cell Biol.*, **20**, 698–714.
9. Harding,S.M., Boiarsky,J.A. and Greenberg,R.A. (2015) ATM dependent silencing links nucleolar chromatin reorganization to DNA damage recognition. *Cell Rep.*, **13**, 251–259.
10. van Sluis,M. and McStay,B. (2015) A localized nucleolar DNA damage response facilitates recruitment of the homology-directed repair machinery independent of cell cycle stage. *Genes Dev.*, **29**, 1151–1163.
11. Kudo,K., Gavin,E., Das,S., Amable,L., Shevde,L.A. and Reed,E. (2012) Inhibition of Gli1 results in altered c-Jun activation, inhibition of cisplatin-induced upregulation of ERCC1, XPD and XRCC1, and inhibition of platinum-DNA adduct repair. *Oncogene*, **31**, 4718–4724.
12. Mazumdar,T., Devecchio,J., Agyeman,A., Shi,T. and Houghton,J.A. (2011) Blocking Hedgehog survival signaling at the level of the GLI genes induces DNA damage and extensive cell death in human colon carcinoma cells. *Cancer Res.*, **71**, 5904–5914.
13. Teichman,J., Dodbiba,L., Thai,H., Fleet,A., Morey,T., Liu,L., McGregor,M., Cheng,D., Chen,Z., Darling,G. *et al.* (2018) Hedgehog inhibition mediates radiation sensitivity in mouse xenograft models of human esophageal adenocarcinoma. *PLoS One*, **13**, e0194809.
14. Das,S., Harris,L.G., Metge,B.J., Liu,S., Riker,A.I., Samant,R.S. and Shevde,L.A. (2009) The hedgehog pathway transcription factor GLI1 promotes malignant behavior of cancer cells by up-regulating osteopontin. *J. Biol. Chem.*, **284**, 22888–22897.
15. Li,H. and Durbin,R. (2009) Fast and accurate short read alignment with Burrows-Wheeler transform. *Bioinformatics*, **25**, 1754–1760.
16. Zhang,Y., Liu,T., Meyer,C.A., Eeckhoute,J., Johnson,D.S., Bernstein,B.E., Nusbaum,C., Myers,R.M., Brown,M., Li,W. *et al.* (2008) Model-based analysis of ChIP-Seq (MACS). *Genome Biol.*, **9**, R137.
17. Robinson,J.T., Thorvaldsdottir,H., Winckler,W., Guttman,M., Lander,E.S., Getz,G. and Mesirov,J.P. (2011) Integrative genomics viewer. *Nat. Biotechnol.*, **29**, 24–26.
18. Hacot,S., Coute,Y., Belin,S., Albaret,M.A., Mertani,H.C., Sanchez,J.C., Rosa-Calatrava,M. and Diaz,J.J. (2010) Isolation of nucleoli. *Curr. Protoc. Cell Biol.*, **47**, 3.36.1–3.36.10.
19. Sasaki,H., Hui,C., Nakafuku,M. and Kondoh,H. (1997) A binding site for Gli proteins is essential for HNF-3beta floor plate enhancer activity in transgenics and can respond to Shh in vitro. *Development*, **124**, 1313–1322.
20. Zhuang,J., Zhang,J., Willers,H., Wang,H., Chung,J.H., van Gent,D.C., Hallahan,D.E., Powell,S.N. and Xia,F. (2006) Checkpoint kinase 2-mediated phosphorylation of BRCA1 regulates the fidelity of nonhomologous end-joining. *Cancer Res.*, **66**, 1401–1408.
21. Sulkowski,P.L., Corso,C.D., Robinson,N.D., Scanlon,S.E., Purshouse,K.R., Bai,H., Liu,Y., Sundaram,R.K., Hegan,D.C., Fons,N.R. *et al.* (2017) 2-Hydroxyglutarate produced by neomorphic IDH mutations suppresses homologous recombination and induces PARP inhibitor sensitivity. *Sci. Transl. Med.*, **9**, eaal2463.
22. Peltonen,K., Colis,L., Liu,H., Trivedi,R., Moubarek,M.S., Moore,H.M., Bai,B., Rudek,M.A., Bieberich,C.J. and Laiho,M. (2014) A targeting modality for destruction of RNA polymerase I that possesses anticancer activity. *Cancer Cell*, **25**, 77–90.
23. Berkovich,E., Monnat,R.J. Jr and Kastan,M.B. (2007) Roles of ATM and NBS1 in chromatin structure modulation and DNA double-strand break repair. *Nat. Cell Biol.*, **9**, 683–690.
24. Kinzler,K.W. and Vogelstein,B. (1990) The GLI gene encodes a nuclear protein which binds specific sequences in the human genome. *Mol. Cell. Biol.*, **10**, 634–642.
25. Li,X., Wang,W., Wang,J., Malovannaya,A., Xi,Y., Li,W., Guerra,R., Hawke,D.H., Qin,J. and Chen,J. (2015) Proteomic analyses reveal distinct chromatin-associated and soluble transcription factor complexes. *Mol. Syst. Biol.*, **11**, 775.
26. Panier,S. and Boulton,S.J. (2014) Double-strand break repair: 53BP1 comes into focus. *Nat. Rev. Mol. Cell Biol.*, **15**, 7–18.
27. Amakye,D., Jagani,Z. and Dorsch,M. (2013) Unraveling the therapeutic potential of the Hedgehog pathway in cancer. *Nat. Med.*, **19**, 1410–1422.
28. Habib,J.G. and O'Shaughnessy,J.A. (2016) The hedgehog pathway in triple-negative breast cancer. *Cancer Med.*, **5**, 2989–3006.
29. Noman,A.S., Uddin,M., Rahman,M.Z., Nayeem,M.J., Alam,S.S., Khatun,Z., Wahiduzzaman,M., Sultana,A., Rahman,M.L., Ali,M.Y *et al.* (2016) Overexpression of sonic hedgehog in the triple negative breast cancer: clinicopathological characteristics of high burden breast cancer patients from Bangladesh. *Sci. Rep.*, **6**, 18830.
30. Liedtke,C., Mazouni,C., Hess,K.R., Andre,F., Tordai,A., Mejia,J.A., Symmans,W.F., Gonzalez-Angulo,A.M., Hennessy,B., Green,M. *et al.* (2008) Response to neoadjuvant therapy and long-term survival in patients with triple-negative breast cancer. *J. Clin. Oncol.*, **26**, 1275–1281.
31. Baserga,S.J., DiMario,P.J. and Duncan,F.E. (2020) Emerging roles for the nucleolus 2019. *J. Biol. Chem.*, **295**, 5535–5537.